JOURNAL OF AIRCRAFT
Vol. 42, No. 6, November–December 2005

Off-Design Reynolds Number Effects for a Supersonic Transport

Lewis R. Owens,* Richard A. Wahls,† and S. Melissa Rivers‡
NASA Langley Research Center, Hampton, Virginia 23681-2199

A high-Reynolds-number wind-tunnel investigation was conducted to assess Reynolds-number effects on the aerodynamic performance characteristics of a realistic, second-generation, supersonic transport concept. The tests included longitudinal studies at transonic and low-speed, high-lift conditions across a range of chord Reynolds numbers (8×10^6 to 120×10^6). Results presented focus on Reynolds-number and static aeroelastic sensitivities at Mach 0.30 and 0.90 for a configuration without a tail. Static aeroelastic effects, which mask Reynolds-number effects, were observed. Reynolds-number effects were generally small, and the drag data followed established trends of skin friction as a function of Reynolds number. Wing boundary layers thinned as Reynolds number increased producing a more nose-down pitching moment because of the increased effective wing camber. This study extends the existing Reynolds-number database for supersonic transports operating at off-design conditions.

Nomenclature

AR	=	aspect ratio, $AR = b^2/S$
b	=	wing span, in.
C	=	local chord length, in.
C_p^*	=	critical pressure coefficient
C_D	=	drag coefficient
C_{Dm}	=	minimum drag coefficient
$C_{F,\mathrm{sf}}$	=	nacelle internal skin-friction drag coefficient (one nacelle) normalized by S
C_L	=	lift coefficient
C_{Lm}	=	lift coefficient at minimum drag coefficient value
$C_{L\alpha}$	=	lift-curve slope, per degree
C_M	=	pitching-moment coefficient referenced to 0.50 mac
C_{MCL}	=	pitch stability
C_p	=	pressure coefficient
CI_{95}	=	95% confidence interval
e	=	Oswald efficiency factor, $= (C_L - C_{\mathrm{Lm}})^2/(C_D - C_{\mathrm{Dm}}) \times [1/(\pi AR)]$
M	=	Mach number
nac	=	engine nacelle
P_T	=	total pressure, psi
q	=	dynamic pressure, psf
Rn	=	Reynolds number based on mac
r	=	local leading-edge radius, in.
S	=	wing reference area, in.^{2}
T_T	=	total temperature, °F
$t_{\max}$	=	local maximum airfoil thickness, inches
α	=	angle of attack, deg
η	=	nondimensional semispan station
θ	=	sectional wing twist change, relative to wind-off twist, deg

Introduction

GROUND-TO-FLIGHT scaling remains one of the challenges facing today's designers of aerospace vehicles. The goal of ground-to-flight scaling is the preflight prediction of aerodynamic characteristics with sufficient accuracy to meet both performance guarantees and certification requirements. Specific challenges, experiences, and suggested approaches for ground-to-flight scaling have been documented extensively over the years for a variety of vehicle classes.[1,2] Reynolds-number effects are among many of the factors affecting successful ground-to-flight scaling.[3–6] The Reynolds number is the ratio of inertial to viscous forces and is the primary aerodynamic scaling parameter used to relate subscale wind-tunnel models to full-scale aircraft in flight. The challenge of Reynolds-number scaling increases as the size of a full-scale aircraft increases. So, the increment between the conventional wind-tunnel Reynolds number and the flight Reynolds number expands. Additionally, the challenge for both wind-tunnel and computational approaches increases as flow features become dominated by viscous-sensitive phenomena such as boundary-layer transition, shock/boundary-layer interaction, and separation onset and progression.

The supersonic transport configuration geometry tested was provided by Boeing and represented a Mach 2.4, 300-passenger aircraft design with a 5000-n mile range. The current study, one of many studies utilizing this reference configuration during NASA's High-Speed Research,[7] targeted improved understanding and prediction of scale effects to reduce risk in the design and development of future vehicles by identifying physical features and associated flow physics of this vehicle class that could contribute to the aerodynamic differences between a full-scale flight vehicle and wind-tunnel models of various scale. A specific focus was directed toward the off-design challenges[8] of efficient transonic cruise and acceleration and quiet high-performance takeoff and landing. For this class of vehicle, a nominal mission profile would require minimum chord Reynolds numbers of approximately 130×10^6 at $M = 0.30$ and 120×10^6 at $M = 0.90$ (Refs. 9 and 10). Conventional ground facilities with appropriately sized models of this type cannot obtain chord Reynolds numbers any higher than about 10 to 30×10^6.

A series of wind-tunnel tests was performed in the National Transonic Facility (NTF) at the NASA Langley Research Center across a wide range of Reynolds numbers. The Reynolds numbers spanned from those available in conventional wind tunnels to those near flight conditions at subsonic and transonic Mach numbers. The tests included longitudinal and lateral/directional studies with and without a tail at transonic and low-speed, high-lift conditions. This paper includes results focused on the Reynolds-number sensitivities of the longitudinal characteristics at subsonic, off-design conditions (Mach 0.30 and 0.90) representative of takeoff and transonic cruise for the configuration without a tail.

Experimental Approach

Model Description

The wind-tunnel model is a 2.2% scale representation of the High Speed Research Program[7] baseline configuration known as

Presented as Paper 2001-0911 at the AIAA 39th Aerospace Sciences Meeting and Exhibit, Reno, NV, 8–11 January 2001; received 27 April 2004; revision received 22 April 2005; accepted for publication 23 April 2005.

*Aerospace Engineer, Flow Physics and Control Branch. Senior Member AIAA.
†Assistant Head, Configuration Aerodynamics Branch. Associate Fellow AIAA.
‡Aerospace Engineer, Configuration Aerodynamics Branch. Member AIAA.

Reference H. This paper focuses on results obtained for the wing/body configuration with the body truncated slightly aft of the wing trailing edge. Figure 1a shows a planform drawing of the model with wing pressure taps and other reference locations noted. The model has a cranked-delta-wing planform with an aspect ratio of 2.367, a span of 34.22 in., and a mean aerodynamic chord of 22.71 in. The inboard wing ($\eta \leq 0.522$) has a blunt ($r/c \sim 0.0025$ to 0.0030) subsonic leading edge with a sweep change from 76 to 68.5 deg at $\eta = 0.226$, a twist varying from approximately 1 deg near $\eta = 0.10$ to -2 deg near $\eta = 0.50$, and variable thickness ratio $t_{\max}/c$ from 0.043 to 0.024. The outboard, supersonic leading edge is sharp, swept 48 deg, has a constant twist of -1.6 deg for $\eta \geq 0.65$, and a constant thickness ratio of 0.024. The reference area for the model is 494.78 in.^{2}. Table 1 provides several key ratios relating the model size to the NTF test section. The model size was selected to minimize support system and wall interference effects.

Table 1 Model size relative to the NTF test section

Ratios	Values
Model wing reference area to NTF cross-sectional area	0.0515
Model span to NTF test-section width	0.3478
Model frontal area to NTF cross-sectional area ($\alpha = 0$ deg)	0.0022

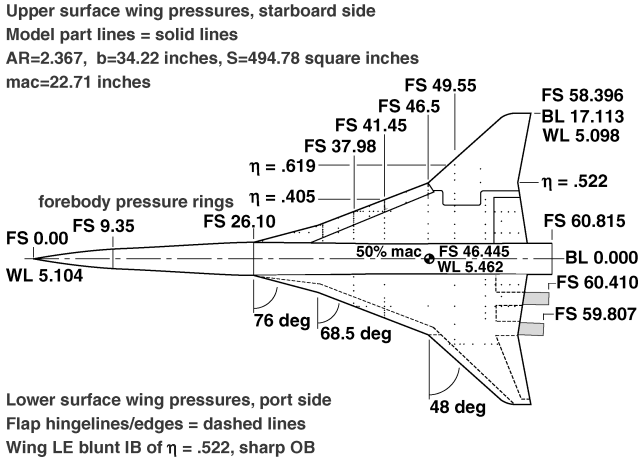

a) Model drawing with pressure locations (linear dimensions in inches)

b) 2.2% Reference H transonic cruise configuration

c) 2.2% Reference H take-off configuration

Fig. 1 Supersonic transport model in the NTF.

The model was designed and constructed specifically for testing in the cryogenic, pressurized conditions of the NTF, where dynamic pressures reached approximately 2700 psf during these tests at transonic conditions; the unloaded model shape was that of the Mach 2.4 cruise, design point. The model was built of maraging steel with a surface finish of 8–16 μ-in. (rms) and a contour tolerance of ± 0.005 in. Photographs (Figs. 1b and 1c) show the model mounted in the NTF test section on a straight support sting. This sting mounts to a 6-deg offset stub sting, which in turn mounts to the facility arc sector resulting in a model angle-of-attack range from -4 to 24 deg.

The model has multiple inboard leading- and trailing-edge parts, multiple outboard wing panels each with different leading- and trailing-edge deflections, and four detachable, 8.43-in.-long, constant internal diameter (1.236 in.), circular flow-through nacelles with boundary-layer diverters located between the wing and nacelle. The inboard nacelles are rigged with toe-in and pitch (nose-down) angles of 1 and 4.17 deg, respectively; the outboard nacelles are rigged with toe-in and pitch angles of 2.4 and 2.84 deg, respectively. The multiple leading- and trailing-edge parts in combination with the multiple outboard panels enabled testing of a variety of configurations including the baseline (supersonic cruise), takeoff, landing, stall recovery, and transonic cruise configurations as defined in Table 2.

The model was instrumented with 48 forebody pressures distributed circumferentially at two fuselage stations and 146 wing pressures distributed in both spanwise and chordwise rows on the starboard upper and port lower surfaces of the wing, as shown in Fig. 1a. A more detailed description of the spanwise pressure orifice locations are listed in Tables 3 and 4 for reference. Additionally, the pressure instrumentation included an internal Preston tube and six nacelle base pressure orifices enabling correction for nacelle internal skin-friction and base drag effects.

For the nacelle internal skin-friction drag corrections, it was assumed that the boundary-layer flow inside each nacelle behaved similarly to a zero-pressure gradient, flat-plate turbulent boundary layer because of the placement of a grit ring just downstream (0.3 in.) of the nacelle inlet lip. The thickness of this turbulent boundary layer developing inside the nacelles changed as Reynolds number increased. Some representative nacelle internal skin-friction force coefficient data for one nacelle are shown in Fig. 2 for both high-lift and transonic conditions. The Preston tube results were calculated from the delta pressure measurement at a point inside the nacelle where it is expected that the local skin-friction value corresponds to the average skin-friction value. This position was estimated to occur at a location of about one-third of the nacelle length. The force coefficient for the Preston tube result is the local skin friction multiplied by the ratio of the internal nacelle wetted area to the wing reference area so that the corrections are directly applicable to the model force/moment coefficients.

There are two main points to consider for the representative data presented in Fig. 2. First, consider the comparison between the Preston tube result and the equivalent flat-plate calculation at each Reynolds-number test condition. Both methods demonstrate comparable skin-friction force coefficient levels as well as a similar trend of change with increasing Reynolds number. Note that the Preston tube results can become nonlinear. For the Mach 0.30 condition, the appearance of nonlinearity occurred at the higher angles of attack and is likely associated with some flow separation on the wing.

Table 2 Available wing configurations

Designation	LE deflection, deg inboard/outboard[a]	TE deflection, deg inboard/outboard[b]
Baseline	0/0	0/0
Takeoff	30/30	10/10
Landing	30/30	20/20
Stall recovery	50/50	30/30
Transonic cruise	0/10	0/3

[a]LE = leading edge. [b]TE = trailing edge.

Table 3 Wing spanwise pressure orifice locations, high-lift configuration

Wing surface	F.S.	Baseline local, $b/2$	$2y/b$													
Upper	34.245	4.082	0.517	0.656	0.694	0.748	0.816	0.858	0.903	0.919	0.940	0.964	——	——	——	——
Upper	36.11	4.818	0.631	0.784	0.951	——	——	——	——	——	——	——	——	——	——	——
Upper	37.98	5.556	0.410	0.547	0.619	0.692	0.735	0.772	0.816	0.858	0.896	0.933	0.948	0.963	0.971	——
Lower	37.98	5.556	0.373	0.547	0.671	0.896	0.947	——	——	——	——	——	——	——	——	——
Upper	39.706	6.238	0.830	0.898	0.967	——	——	——	——	——	——	——	——	——	——	——
Lower	39.706	6.238	0.851	——	——	——	——	——	——	——	——	——	——	——	——	——
Upper	41.45	6.925	0.337	0.516	0.591	0.694	0.801	0.844	0.871	0.892	0.913	0.927	0.942	0.955	0.975	——
Lower	41.45	6.925	0.439	0.663	0.738	0.802	0.860	0.893	0.924	0.957	——	——	——	——	——	——
Upper	43.982	7.926	0.699	0.858	0.969	——	——	——	——	——	——	——	——	——	——	——
Upper	46.5	8.912	0.268	0.341	0.457	0.622	0.707	0.794	0.831	0.875	0.899	0.926	0.954	0.966	0.978	0.989
Lower	46.5	8.912	0.623	——	——	——	——	——	——	——	——	——	——	——	——	——
Upper	49.55	11.655	0.260	0.350	0.476	0.598	0.654	0.796	0.857	0.909	——	——	——	——	——	——
Lower	49.55	11.655	0.261	0.476	0.660	0.804	0.854	——	——	——	——	——	——	——	——	——
Upper	53.16	14.906	0.160	0.204	0.273	0.372	0.423	0.599	0.712	——	——	——	——	——	——	——
Lower	53.16	14.906	0.160	0.203	0.291	0.373	0.423	0.467	0.668	——	——	——	——	——	——	——

Table 4 Wing spanwise pressure orifice locations, transonic configuration

Wing surface	F.S.	Baseline local, $b/2$	$2y/b$													
Upper	34.245	4.082	0.517	0.658	0.696	0.747	0.815	0.896	0.937	0.974	1.00	——	——	——	——	——
Upper	36.11	4.818	0.631	0.738	0.978	——	——	——	——	——	——	——	——	——	——	——
Upper	37.98	5.556	0.410	0.547	0.619	0.692	0.735	0.773	0.838	0.887	0.936	0.958	0.981	1.00	——	——
Lower	37.98	5.556	0.373	0.547	0.671	0.923	0.985	——	——	——	——	——	——	——	——	——
Upper	39.706	6.238	0.797	0.890	0.983	——	——	——	——	——	——	——	——	——	——	——
Lower	39.706	6.238	0.891	——	——	——	——	——	——	——	——	——	——	——	——	——
Upper	41.45	6.925	0.337	0.516	0.591	0.694	0.802	0.857	0.884	0.930	0.950	0.968	0.985	1.00	——	——
Lower	41.45	6.925	0.439	0.663	0.738	0.802	0.876	0.912	0.950	0.988	——	——	——	——	——	——
Upper	43.982	7.926	0.699	0.840	0.986	——	——	——	——	——	——	——	——	——	——	——
Upper	46.5	8.912	0.268	0.341	0.457	0.622	0.707	0.794	0.831	0.861	0.900	0.930	0.961	0.977	1.00	——
Lower	46.5	8.912	0.623	——	——	——	——	——	——	——	——	——	——	——	——	——
Upper	49.55	11.655	0.260	0.350	0.476	0.598	0.653	0.795	0.856	0.909	——	——	——	——	——	——
Lower	49.55	11.655	0.261	0.476	0.660	0.804	0.853	——	——	——	——	——	——	——	——	——
Upper	53.16	14.906	0.160	0.204	0.273	0.372	0.423	0.599	0.711	——	——	——	——	——	——	——
Lower	53.16	14.906	0.160	0.203	0.291	0.373	0.423	0.467	0.667	——	——	——	——	——	——	——

The angle of attack where the nonlinearity starts shifted to higher angles of attack as the Reynolds number increased. For the Mach 0.90 condition, the nonlinearity tended to be most significant for the intermediate Reynolds-number condition. However, even with this nonlinear behavior the Reynolds-number trends are clear and show the effect of internal nacelle skin-friction reduction as the boundary layer inside the nacelle thins with increasing Reynolds number. Second, the favorable comparisons between these two methods of determining the nacelle internal skin friction over the wide range of test conditions led to the assumption that using the equivalent flat-plate method was appropriate to correct for this internal nacelle effect.

The thinning of the nacelle internal boundary layers with increasing Reynolds number certainly had an impact on the nacelle spillage drag as the amount of mass flow through each nacelle also increased. However, no attempt was made to characterize or correct for the change in the spillage drag with Reynolds number. The flow-through nacelles were also removed to install a boundary-layer rake on the underside of the wing at the position where the inboard nacelle inlet was located. This inlet rake configuration was tested to see if the wing boundary layer ever became thick enough to be ingested in the flow-through nacelle. The inboard nacelle position was selected for the inlet rake measurements because it had the longest run of wing boundary layer and seemed the most likely candidate for potential boundary-layer ingestion. The results of the inlet rake testing showed no indications of the wing lower surface boundary layer becoming thick enough to be ingested in the inboard nacelle with the given nacelle boundary-layer diverter design.

Further details about the instrumentation, data reduction, and corrections are presented in Refs. 9–14. Additional test and facility details are included in Refs. 9, 10, 15–18.

Test Conditions

The NTF enables testing across a wide range of Reynolds numbers from those available in conventional wind tunnels to those near flight conditions at subsonic and transonic Mach numbers. Tests of the supersonic transport model spanned Mach numbers from 0.30 to 1.10 and chord Reynolds numbers from 8×10^6 to 120×10^6 based on the mean aerodynamic chord. Figure 3 provides the NTF operational envelopes for Mach 0.30 and 0.90. Note that each envelope plot also shows the specific test condition points associated with the data presented from this investigation.

The goals of assessing Reynolds-number scale effects and extrapolating to flight conditions required a series of intermediate conditions to better identify the trends. As seen in Fig. 3, the desired Reynolds-number range could not be covered using a constant total pressure (dynamic pressure). However, the independent control of total pressure, total temperature, and fan speed in the NTF allow the isolation of viscous (Reynolds-number) effects, static aeroelastic (dynamic pressure) effects, and compressibility (Mach) effects. Several conditions are used to isolate static aeroelastic effects from the viscous effects for Mach 0.30 and 0.90 as shown in Fig. 3. During Reynolds number sweeps, the ratio of dynamic pressure q to the model material modulus of elasticity E is held constant. This is done to maintain a constant static aeroelastic state q/E because of the variability of the model material modulus of elasticity over the temperature range of the NTF. Note that constant q/E was not maintained for the two lowest Reynolds-number conditions at Mach 0.30 because of the use of the air mode of testing rather than the nitrogen mode. However, the aeroelastic adjustment methodology (as explained in the Results and Discussion section) is sufficient to provide the Reynolds-number effects at this lower dynamic pressure level.

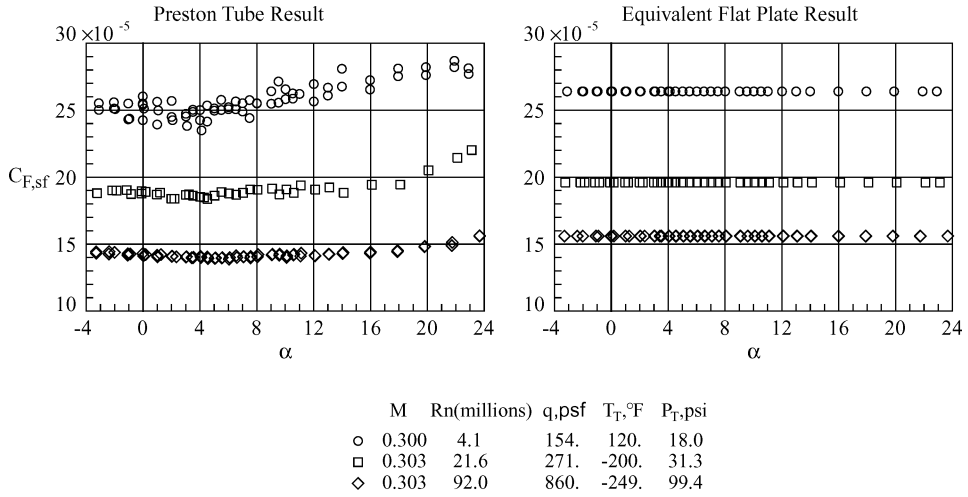

a) Take-off conditions

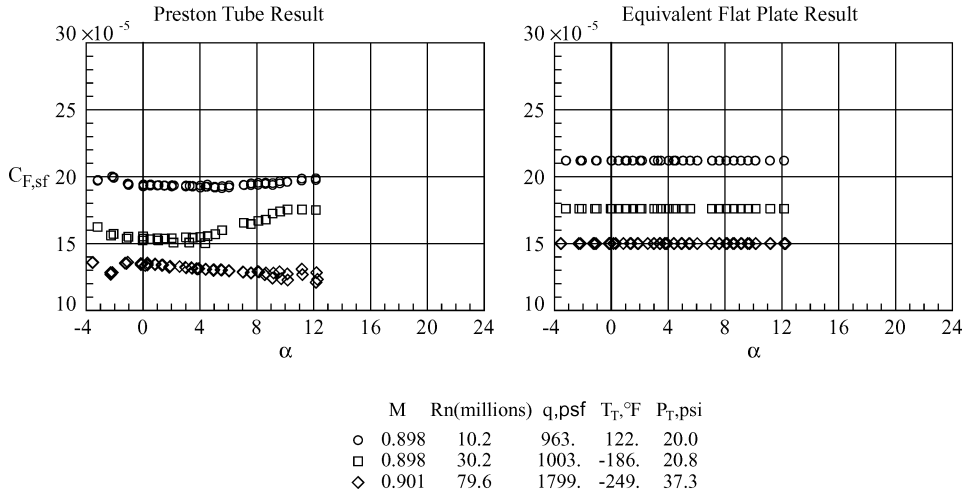

b) Transonic cruise conditions

Fig. 2 Reynolds-number effect on inboard nacelle internal skin-friction force coefficient with α.

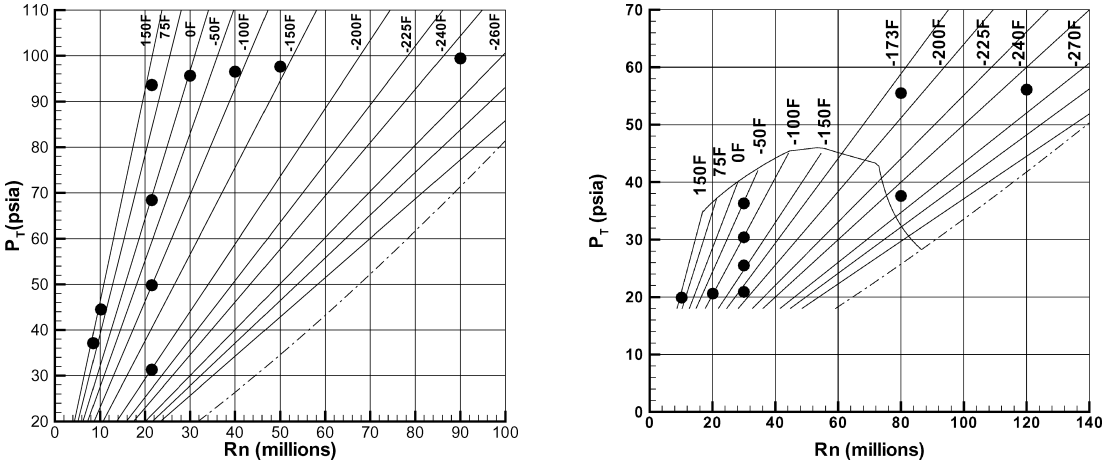

a) Mach = 0.30 **b) Mach = 0.90**

Fig. 3 NTF operational envelopes.

Boundary-Layer Transition

Boundary-layer transition on the wing was allowed to occur naturally, in general, to observe transition effects over the complete Reynolds-number range. Limited data were acquired with a forced transition pattern on the wing at low-Reynolds-number test conditions. The wing boundary-layer tripping pattern consisted of 0.125 in. wide carborundum grit strips that were placed on both the upper- and lower-wing surfaces. These grit strips were locally parallel to the wing leading edge and were placed 0.625 in. (measured stream-wise) downstream of the wing leading edge. When applied, these wing trips were only used on wing configurations with little or no leading-edge flap deflections because of the uncertainty in locating the trips with highly deflected leading-edge flaps. Throughout all testing, the transition location was consistently fixed on the forebody with a ring of carborundum grit located 1.5 in. from the nose, and a nacelle internal surface grit ring located 0.3 in. downstream

of the inlet lip to facilitate the internal nacelle drag correction; this approach was applied at all test conditions. All trips were sized and located based on the criteria of Ref. 19.

Results and Discussion

Figure 4 shows representative data for the baseline, takeoff, and transonic cruise configurations at low and high Reynolds numbers and is provided to indicate the general, longitudinal aerodynamic characteristics of the wing/body configuration. The data presented in Fig. 4 include the combined effects of different flap configurations, static aeroelastic deformation, and Reynolds number. The discussion of the results will address static aeroelastic effects and the adjustments to isolate the Reynolds-number (viscous) effects for a given configuration. In these discussions, the angles of attack chosen correspond to takeoff ($\alpha = 9$ deg), transonic cruise ($\alpha = 5$ deg), and minimum drag ($\alpha = 1.1$ deg) conditions.

Experimental Uncertainty

Short-term data repeatability (within test/Mach series) is quantified in terms of a 95% confidence interval.[20] The 95% confidence interval is interpreted as the bounds about an estimated mean (average of multiple, repeat polars) that encompasses the true mean value with a chance of 95%. Examples of the short-term repeatability of longitudinal aerodynamic data are shown in Refs. 9 and 10. For reference, the average 95% confidence intervals for C_L, C_D, and C_M are approximately ± 0.002, ± 0.0003, and ± 0.0005, respectively, and are given here as an uncertainty estimate.

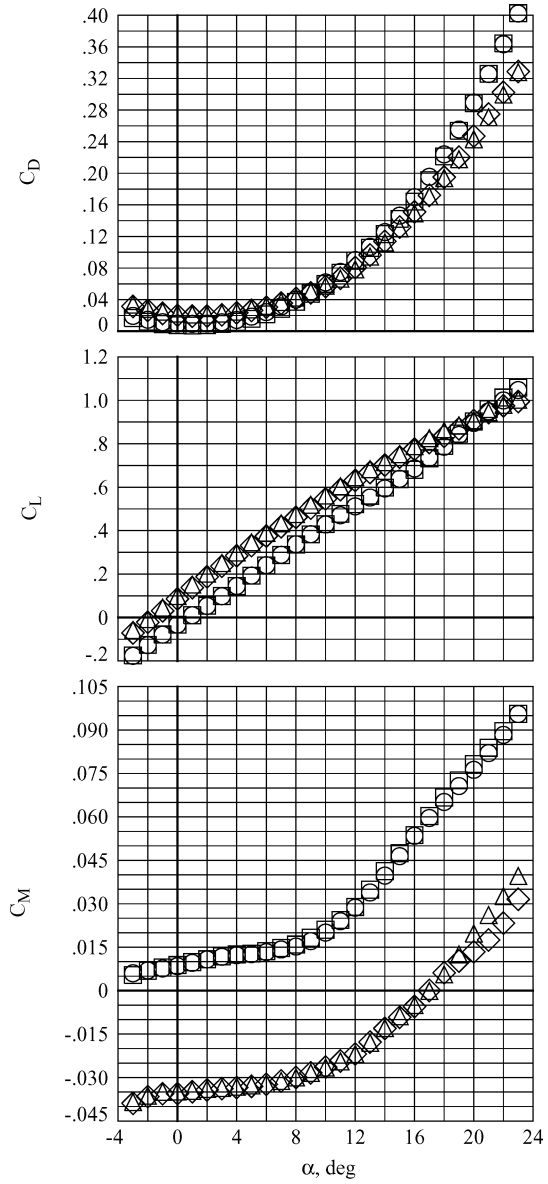

	Rn (millions)	q, psf	config
○	8.5	318.	Baseline + nac
□	90.0	839.	Baseline + nac
◇	8.5	318.	Take-off + nac
△	89.9	842.	Take-off + nac

a) High-lift configurations, $M = 0.30$

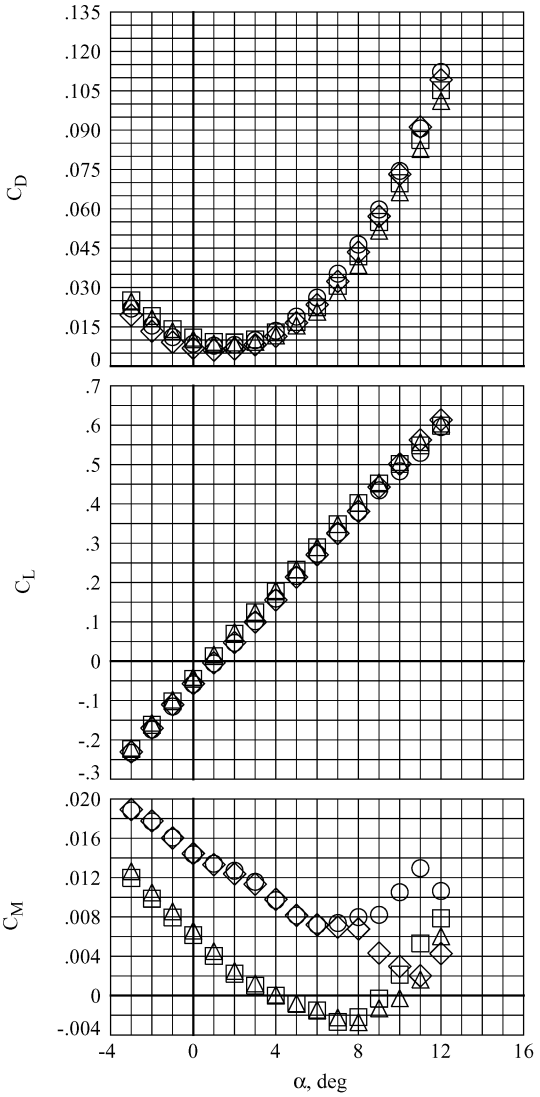

	Rn (millions)	q, psf	config
○	10.2	967.	Baseline + nac
□	10.2	963.	Transonic + nac
◇	79.6	1797.	Baseline + nac
△	79.5	1802.	Transonic + nac

b) Transonic configurations, $M = 0.90$

Fig. 4 Representative longitudinal force and moment data.

The angle-of-attack measurement was made with an internal, heated accelerometer package; quoted accuracy of the package is estimated to be ±0.01 deg.[13] Wing twist measurements were made using a video model deformation system.[14] The system provided sectional twist change data relative to the wind-off shape with a quoted accuracy of ±0.1 deg.

The tunnel Mach number, dynamic pressure, and Reynolds number have uncertainty levels of approximately ±0.002, ±1.5% of reading, and $\pm 0.5 \times 10^6$, respectively. Finally, the wing pressure measurements had an uncertainty level estimated to be within ±1.5% of the pressure coefficient value.

Static Aeroelastic Effects

Achieving high-Reynolds-number conditions approaching those that are characteristic of flight requires the manipulation of both the total temperature and pressure, as seen in Fig. 3. As a result, the static aeroelastic deformation of the model, in particular the wing, under load must be considered when attempting to isolate Reynolds-number effects. Previous reports for high-aspect-ratio subsonic transport configurations have shown the static aeroelastic effects to be on the order of Reynolds-number effects and sometimes opposite in sense to that of Reynolds-number trends, thus masking the Reynolds-number effects.[21,22] Like the subsonic transport configurations, the current low-aspect-ratio supersonic transport model is flexible under load, most notably on the thin outboard wing panels.

Video model deformation measurements of the wing under load were concentrated on the outboard wing panel. These measurements indicated that as the aerodynamic load on the wing increased the outboard wing panel experienced increased washout, similar to that observed on the higher-aspect-ratio subsonic transports. This type of wing bending occurs because the local lifting center of pressure is located behind the elastic axis of the wing, which produces a local nose-down torsional moment at each outboard wing section. Figure 5 shows representative wing twist data at $\eta = 0.922$, relative to the wind-off twist, as a function of dynamic pressure and angle of attack. At the higher dynamic pressures and/or higher angles of attack, the magnitude of the local twist change increases (more nose-down) to about 1 to 2 deg. The relationship between local wing twist change and dynamic pressure is linear for the range of dynamic pressure shown. One would expect that extrapolation to the wind-off condition ($q = 0$ psf) would indicate no twist change; the data at $\alpha = 5$ deg demonstrate this to be the case within the level of measurement uncertainty.

Typical effects of static aeroelastic wing bending on the longitudinal aerodynamic data obtained are presented in Fig. 6. These data were obtained with a constant chord Reynolds number of 30×10^6 for several total pressure (dynamic pressure) conditions, as shown in Fig. 3. The force and moment results show trends consistent with the increasing washout of the wing with increasing load; for a constant body angle of attack, the lift and drag decrease, and the nose-up pitching moment increases with increasing dynamic pressure. The change in pitching moment is driven by the significant lift reduction occurring primarily on the outboard wing, which is aft of the moment reference center. The changes in drag are consistent with the reductions in lift. Typical effects of static aeroelastics on the drag polar are presented in Fig. 7. The changes in C_D and C_L are often such that the drag polar appears unchanged. This can occur even in the presence of significant static aeroelastic effects.

These static aeroelastic effects can also be seen in the changes in the lift-curve slope and the longitudinal stability. For the transonic data, the lift-curve slope decreased by approximately 2.5% at $\alpha = 5$ deg for each configuration over the dynamic pressure range examined. The longitudinal stability decreased as the neutral point moved forward by approximately 0.6% of the mean aerodynamic chord at $\alpha = 5$ deg for the transonic cruise configuration.

The data presented in Fig. 6 are typical of the increments used to adjust data to a constant dynamic pressure to essentially remove static aeroelastic effects from the analysis of Reynolds-number effects. The fundamental assumptions in establishing the adjustment increments are 1) the force and moment variation with dynamic pressure is linear, like the wing twist change; and 2) the sensitivity

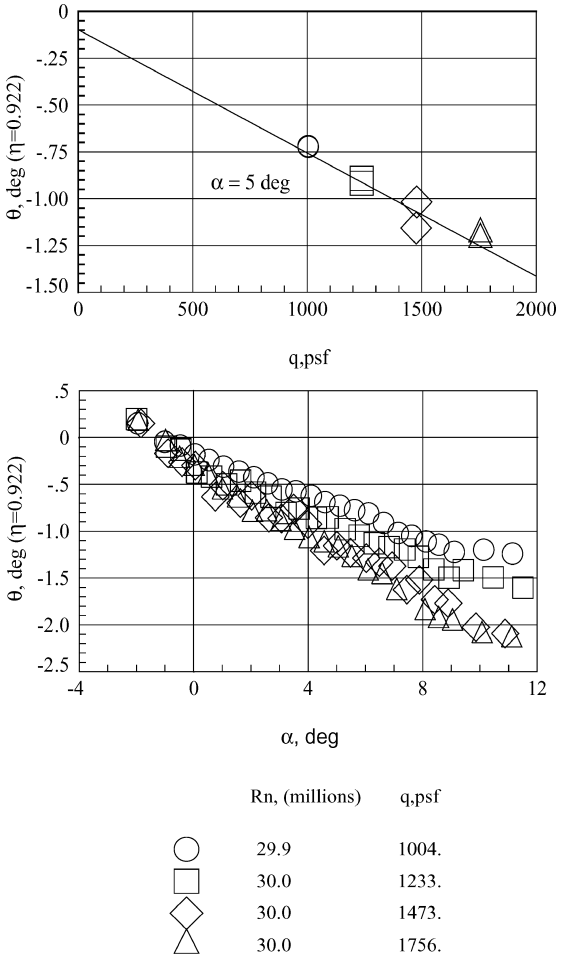

Fig. 5 Outboard wing twist change under load for transonic cruise configuration, $M = 0.90$.

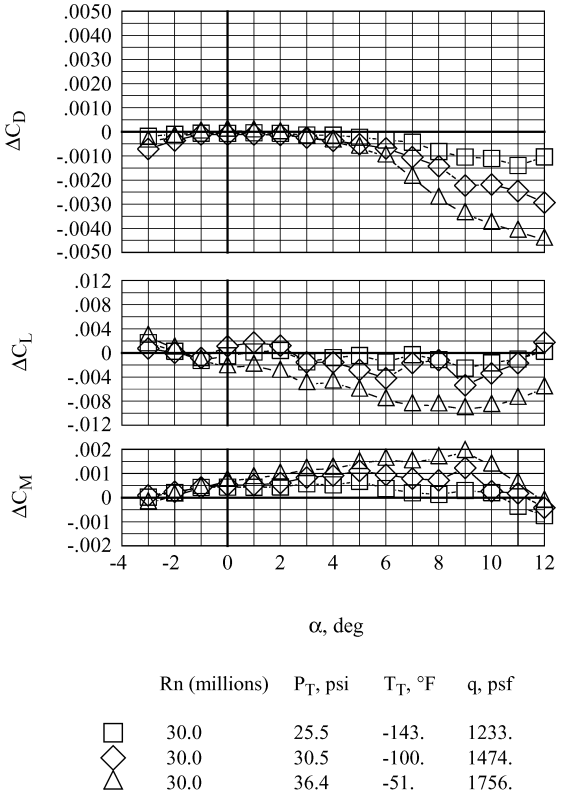

Fig. 6 Static aeroelastic effects on longitudinal coefficients, referenced to $q = 1000$ psf, $M = 0.90$.

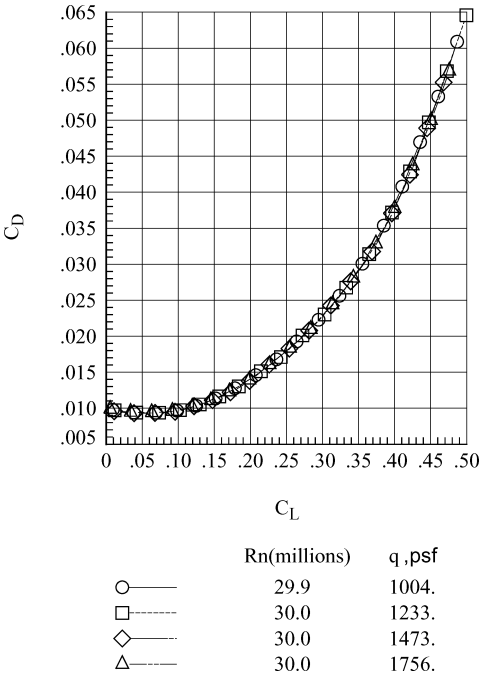

Fig. 7 Static aeroelastic effects on drag polar for transonic cruise configuration, $M = 0.90$.

to dynamic pressure defined at one Reynolds number is valid at other Reynolds numbers. Studies on subsonic transports and analysis of static aeroelastic sensitivity at other Reynolds numbers for this model support these assumptions. As applied in this paper, force and moment coefficient data were adjusted to nominal dynamic pressures of 1000 psf for the transonic configurations and 270 psf for the takeoff configuration. Ideally, an adjustment would be made to shift the coefficient data to the wind-off condition ($q = 0$ psf) to obtain results for the rigid, nondeformed model shape most frequently used in computational simulations. However, the extrapolation to reach the wind-off shape condition introduces additional uncertainty and was not applied herein.

Adjustments for static aeroelastic effects were not applied to any of the wing pressure data presented in this paper. The effect on the wing pressure data is not significant for most of the pressure ports, which were far enough inboard of the wing leading-edge break ($\eta = 0.522$) that the model deformation was minimal.

Reynolds-Number Effects

The primary Reynolds-number effects observed for both the takeoff and the transonic cruise configurations were the skin-friction drag reductions as the Reynolds number increased. The takeoff configuration also experienced a lift increase as the wing boundary layers thinned with increasing Reynolds number because of the increased effective wing camber. This more effective wing camber was also evident in both configurations as the pitching moment became more nose down with the Reynolds-number increase. For the transonic configuration, an increase in longitudinal stability with increasing Reynolds number was also observed. The following discussion will examine the Reynolds-number trends for the longitudinal force and moment coefficients (adjusted for static aeroelastic effects) for the takeoff and transonic cruise configurations at specific angles of attack. Some wing pressure data (not adjusted for aeroelastic effects) will also be introduced to help explain the flow physics that affect the force and moment data.

Low-Speed, High-Lift Conditions

The Reynolds-number effects near the takeoff condition are presented in Fig. 8 for the takeoff configuration. In general, drag decreases as the Reynolds number increases and is accounted for by the theoretical trend of skin-friction reduction with Reynolds number. Theoretical skin-friction drag for the configuration was calcu-

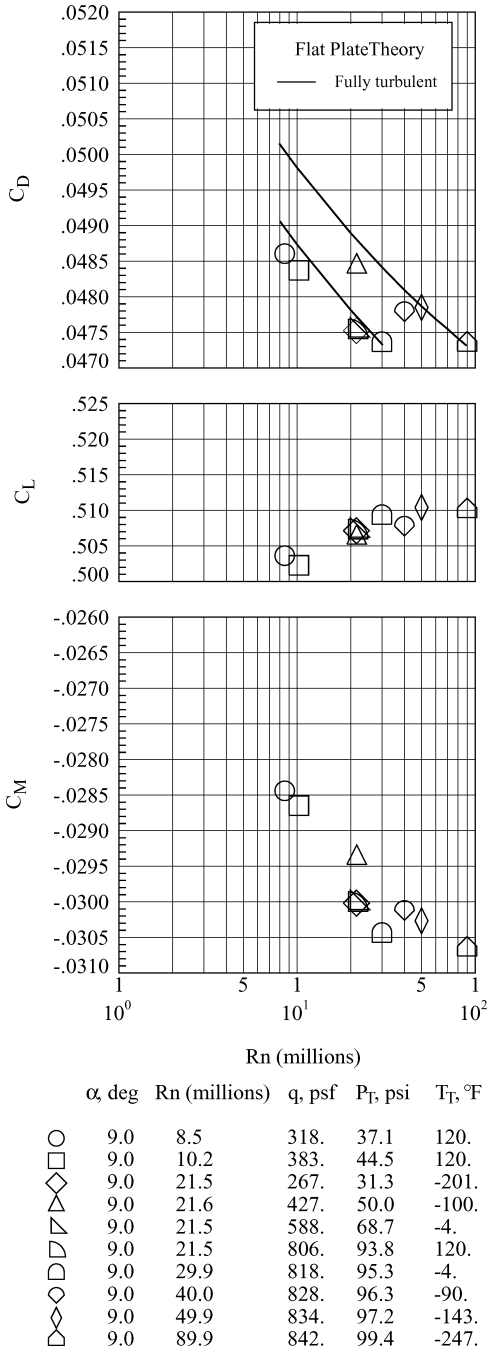

Fig. 8 Longitudinal coefficient trends with Reynolds number, near takeoff point, $M = 0.30$ (with aeroelastic correction).

lated with equivalent flat-plate theory, plus form factors, using the Blasius and Karman–Schoenherr incompressible skin-friction correlations for laminar and turbulent boundary layers, respectively, with compressibility effects accounted for with a reference temperature method.[23] As applied herein, the flat-plate theory assumed that the same extent of laminar flow was present on both the upper and lower outboard wing surfaces and that fully turbulent flow existed on both upper and lower surfaces of the inboard wing. All theoretical data were adjusted by a constant increment such that the fully turbulent theoretical curve was anchored to the experimental data at a high-Reynolds-number condition.

There were two distinct groupings of the measured drag data. One group of data includes Reynolds numbers of 30×10^6 and below (except for the $q = 430$ psf data at $Rn = 21.6 \times 10^6$). The second group contains all higher-Reynolds-number data and the $q = 430$ psf data at $Rn = 21.6 \times 10^6$. The higher-Reynolds-number

group is associated with an increase in the drag level, like a small bias of about 10 counts, over that of the lower-Reynolds-number grouping. The bias is illustrated in Fig. 8 by the increment between the two fully turbulent theoretical curves each anchored by the highest-Reynolds-number data (fully turbulent) within each data grouping. This drag level increase is attributed primarily to an inward movement of the leading-edge separation at a given angle of attack, which produces a vortex lift effect causing a small force and moment level increment. A sketch illustrating the leading-edge separation movement for this biasing effect is shown in Fig. 9. Within each of these two groupings shown in Fig. 8, the drag trend with Reynolds number closely follows the classic trends of skin friction with Reynolds number. This is a Reynolds-number effect, and it is caused by the reduction in skin-friction drag as the Reynolds number increases.

In an attempt to understand the 10 count biasing effect observed in the drag data, an analysis of the wing attachment-line boundary-layer state was performed using representative inboard leading-edge radii at test conditions that span the overlapping regions of the two data groupings. This first-order analysis modeled the wing leading edge as a swept circular cylinder to calculate the attachment-line Reynolds number *Rbar*. Results from this analysis are presented in Fig. 10 along with the two lines that separate the range of attachment-line Reynolds number into three boundary-layer state regions: laminar, intermittent, and turbulent. The lines defining the interfaces between these regions were adapted from the work of Poll and Paisley.[24] In Fig. 10, the attachment-line Reynolds number is calculated for three span-wise stations ($\eta = 0.25$, 0.40, and 0.52) that cover the inboard leading edge. As the chord Reynolds number increases, the attachment-line boundary layer progresses from completely laminar at 8.5×10^6 to almost fully turbulent at 50×10^6. When the attachment-line boundary layer is laminar, it is more

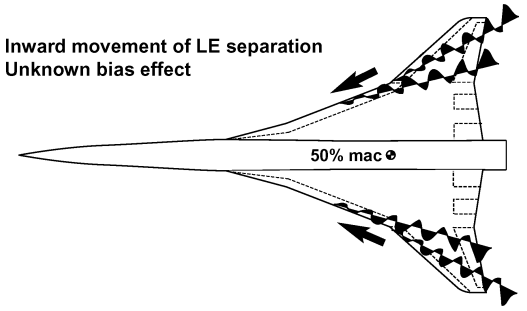

Fig. 9 Leading-edge separation movement with systematic bias.

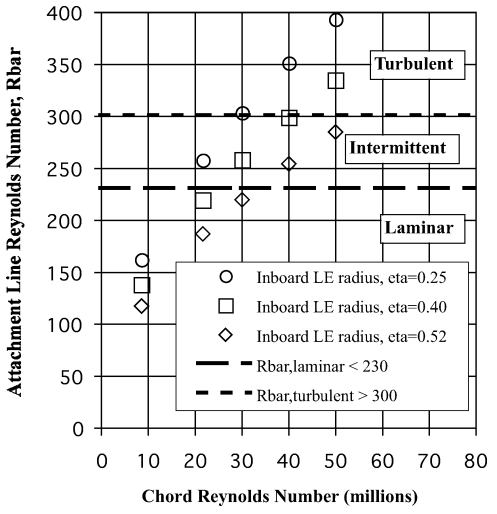

Fig. 10 Wing attachment-line boundary-layer analysis similar to that of Poll and Paisley.[24]

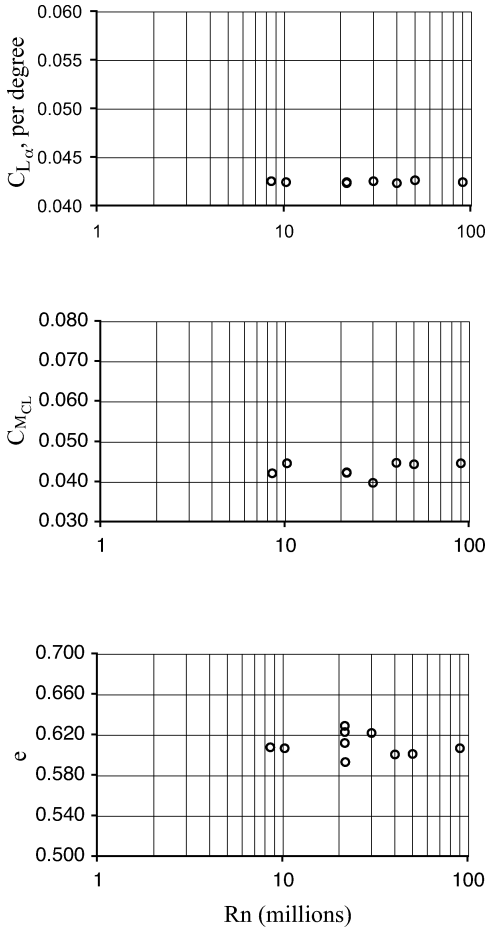

Fig. 12 Lift-curve slope, pitch stability, and Oswald efficiency factor trends with Reynolds-number near takeoff conditions ($\alpha = 9$ deg), $M = 0.30$ (with aeroelastic correction).

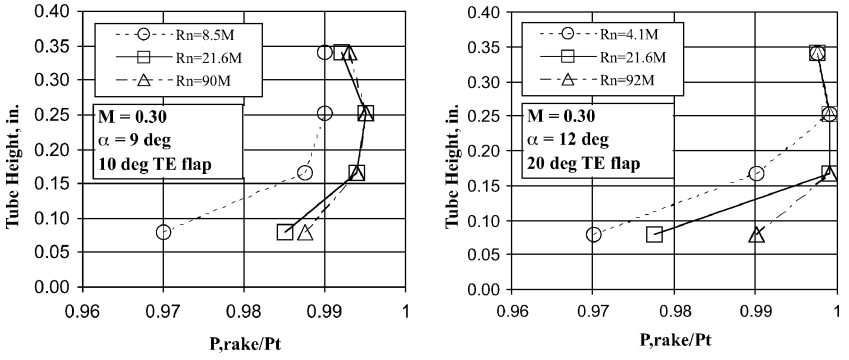

Fig. 11 Trailing-edge flap boundary-layer measurements for the takeoff and landing configurations.

susceptible than either a transitional or turbulent one to separation in the strong adverse pressure gradient associated with the leading-edge region. For the attachment-line boundary-layer model to be consistent with the observed biasing effect, then some mechanism would need to occur to shift the attachment-line boundary layer to a turbulent state at low Reynolds number while also shifting it to a laminar state at the high Reynolds numbers. No definitive mechanisms were identified that might cause this kind of modification to the attachment-line boundary-layer state. More discussion of this biasing effect will be presented later when wing pressure data for these conditions are examined.

The lift trend with Reynolds number near the takeoff condition shows that the lift increases slightly over the range of Reynolds numbers tested. The biasing effect observed in the drag data is not evident in the lift data. This might be caused by either the lift measurement being somewhat less sensitive than the drag measurement or, more likely, the lift distribution on the wing changing with the biasing mechanism such that the net lift remains relatively constant. The overall increase in lift across the Reynolds-numbers range is associated with reducing the wing boundary-layer thickness, which increased the effective wing camber.

Wing trailing-edge flap surface-pressure data were not available for analysis because of model installation/tubing routing difficulties in the very thin model wing trailing-edge regions. However, several high-lift configurations were run with a boundary-layer measurement made at the trailing edge of an inboard trailing-edge flap (Butt line = 3.5 in.). The four-probe boundary-layer rake was built into the flap part, and it was made up of 0.020-in. outside diameter metal tubing spaced above the flap surface approximately every 0.080 of an inch. Each rake tube extended downstream approximately nine tube diameters before turning downward toward the flap lower surface and then eventually entered the model for routing through the lower flap surface. Also, this rake was fabricated so that its thickness was on the order of the tubing diameter. This rake was used to assess the effect of Reynolds number on the trailing-edge flap upper surface boundary layer. Figure 11 illustrates the effect of Reynolds number on the trailing-edge flap boundary layer for two different trailing-edge flap deflections at high-lift conditions. As the Reynolds number increased, the flap boundary layer became thinner. The thinner wing boundary layer enables the flow to see more of the wing camber as the Reynolds number increases.

The pitching-moment trends with Reynolds number are also presented in Fig. 8. As observed in the drag data, the two distinct data groups are also present in the pitching-moment data. Within each of these groups, the trend with increasing Reynolds number is to develop a more nose-down pitching moment. The more nose-down pitching moment with Reynolds number increase is consistent with the camber effect discussed in the preceding lift data discussion. The nose-up level shift between the two data groupings is consistent with an inward movement of the inboard leading-edge separation at a given angle of attack, which is caused by the bias effect illustrated in Fig. 9.

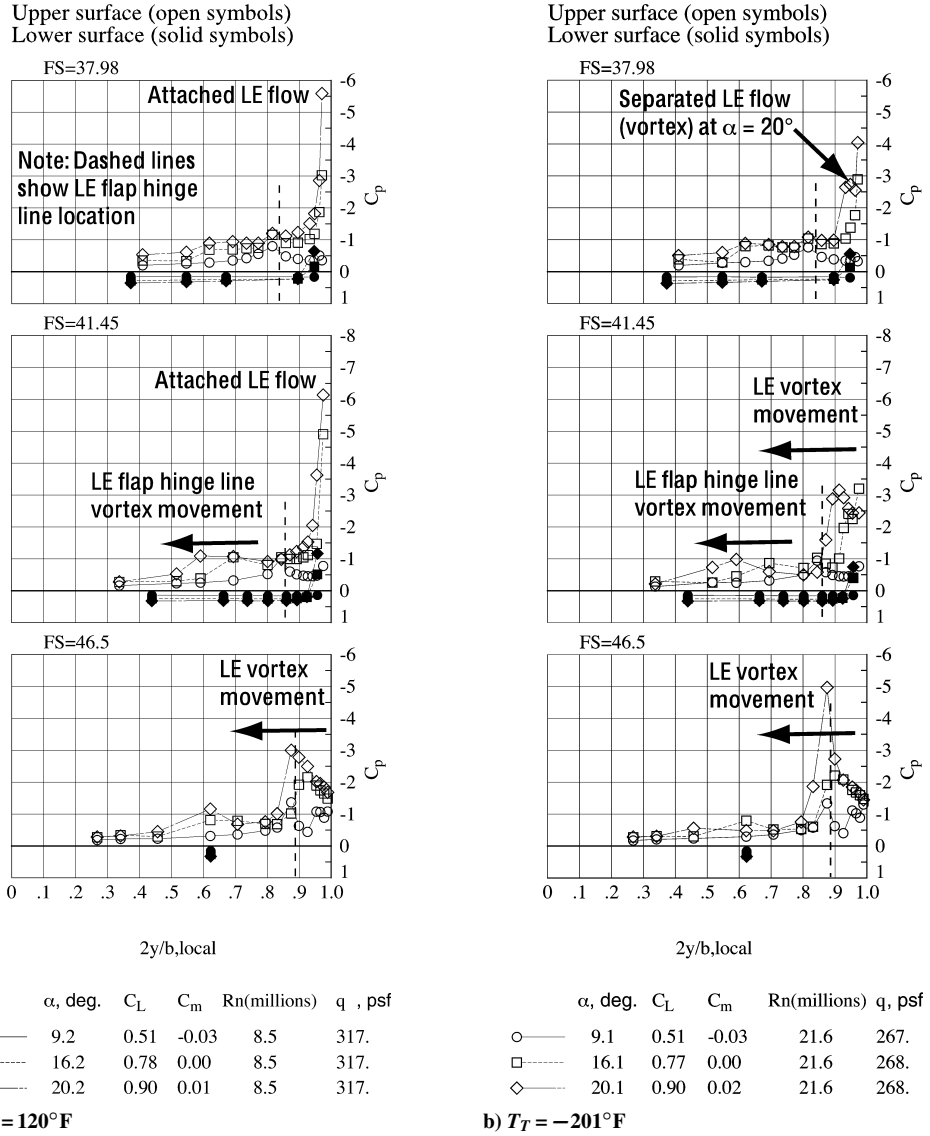

a) $T_T = 120°$F **b) $T_T = -201°$F**

Fig. 13 Vortex flow development with α increase at different Reynolds numbers for the takeoff configuration, $M = 0.30$.

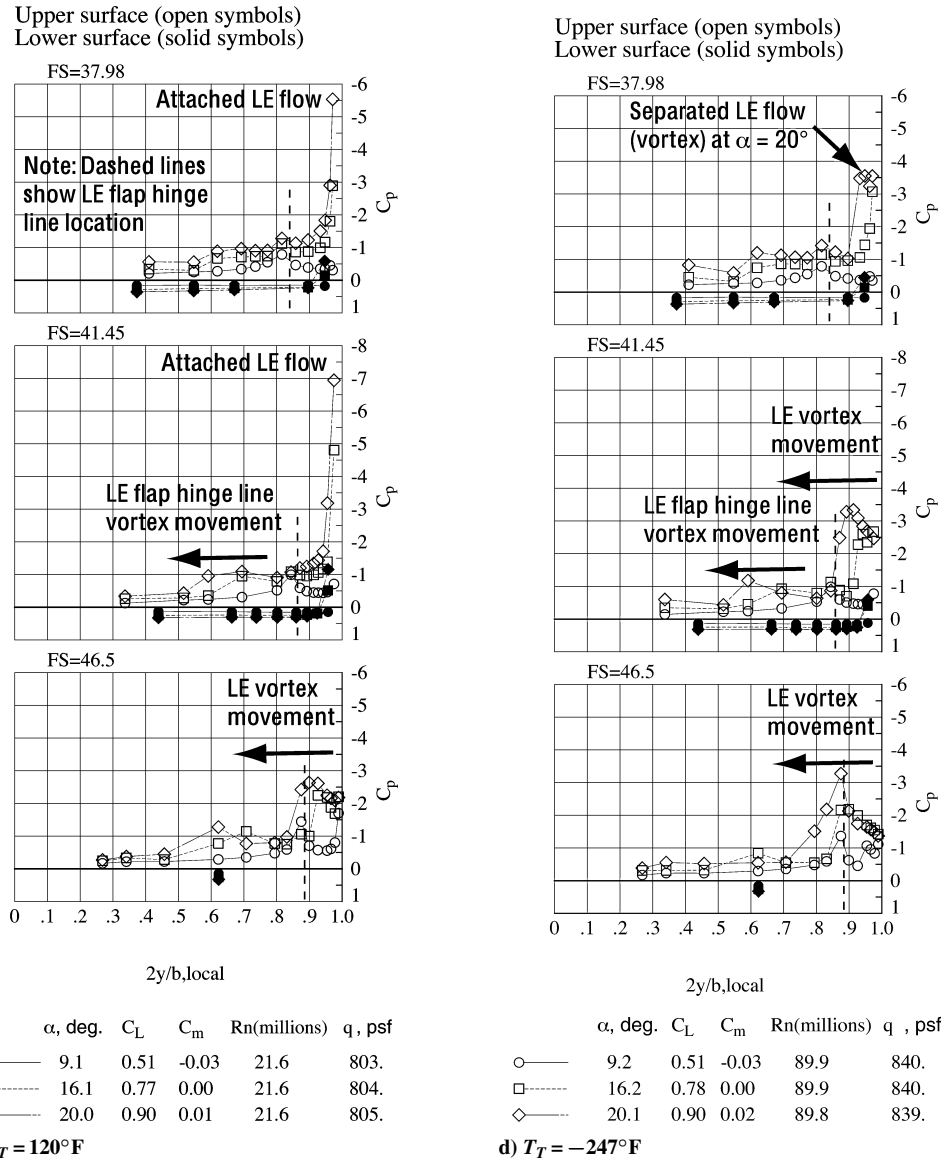

c) $T_T = 120°\text{F}$ **d)** $T_T = -247°\text{F}$

Fig. 13 Vortex flow development with α increase at different Reynolds numbers for the takeoff configuration, $M = 0.30$ (continued).

For reference, the pitching-moment coefficients can be related to the effects of stabilizer deflection for a configuration with a horizontal tail. This relationship is presented to give a perspective on the significance of the Reynolds-number effect on the pitching-moment coefficient. The stabilizer effectiveness for the full configuration with a tail (when closed aftbody and horizontal tails are present) is approximately a 0.005 change in pitching-moment coefficient for 1 deg of stabilizer deflection; one major division on the pitching-moment coefficient plot represents roughly 0.10 deg of stabilizer deflection to compensate for the pitching moment change. For the takeoff configuration, the Reynolds-number effect presented in Fig. 8 is on the order of a 0.4-deg stabilizer change (approximately 1% of stabilizer deflection range) to balance the additional nose-down pitching moment that develops with the Reynolds-number increase.

The effects of Reynolds number on the lift-curve slope, the longitudinal stability, and the drag-polar shape for the takeoff configuration are shown in Fig. 12. The lift-curve slope for the takeoff configuration is essentially constant with a value of approximately 0.042 per degree. So, the increase in lift seen in absolute lift level at the takeoff condition (see Fig. 8) is not associated with a change in the configuration lift-curve slope with Reynolds-number increase. The positive and relatively constant value of C_{MCL} suggests that the takeoff configuration is longitudinally unstable and does not improve over the Reynolds-number range covered in this study.

Finally, to see the change in the drag polar shape with Reynolds number, the trend of the Oswald efficiency factor e with Reynolds number is presented. If this factor is equal to a value of one, then the drag-polar shape is parabolic. For this configuration, this factor is essentially constant over the Reynolds-number range at a value of about 0.61 and is somewhat variable in the aeroelastic sweep region.

Because the force and moment data for the high-lift configurations show a fundamental shift in drag and pitching moment levels between two distinct data groupings, the wing pressures are examined to try and provide insights into the consistency of the patterns discussed above. Note that this fundamental shift was not observed in any of the data obtained for any of the transonic configurations (with or without wing trips).

Some spanwise pressure distributions are shown in Fig. 13 for three fuselage stations corresponding to the inboard wing ($\eta \leq 0.522$). The local wing pressure coefficient is plotted vs a spanwise coordinate normalized by the local span (no leading-edge flap deflection) at that fuselage station. The nondimensional span coordinate equals zero at the model centerline and one at the wing leading edge. Note that the pressures on the wing leading edge fall a little short of $2y/b$, local $= 1.0$ when the leading-edge flap is deflected.

Each pressure distribution plot in Fig. 13 shows the effect of increasing the angle of attack at a given Reynolds number and dynamic pressure test condition. Because these data were obtained on the takeoff configuration, a dotted line is used to indicate the

approximate location of the leading-edge flap hinge line. Also noted on these plots are where vortices occur and the general inboard movement as the angle of attack increases. At the takeoff condition ($\alpha = 9$ deg), the leading-edge flow is attached for the two most inboard pressure stations, fuselage station (F.S.) = 37.98 and 41.45, over the range of test conditions. The most outboard station (F.S. = 46.5) has a separated leading-edge flow at $\alpha = 9$ deg at all test conditions except for that shown in Fig. 13c. Thus, looking at the F.S. = 46.5 leading-edge pressures at $\alpha = 9$ deg in Figs. 13a and 13c might lead one to conclude that the leading-edge vortex moved outboard with the Reynolds-number increase. However, such a conclusion is not supported if the corresponding F.S. = 46.5 pressure data are considered in Figs. 13a and 13b or in Figs. 13a and 13d because the wing leading edge remains separated at $\alpha = 9$ deg for all of these Reynolds-number conditions. This inconsistent behavior can be associated with the static aeroelastic deformation on the outboard wing panel influencing these wing pressures near the wing leading-edge break. Recall that no attempt was made to correct the wing pressure coefficient data for static aeroelastic effects.

At the angles of attack of 16 and 20 deg, the leading-edge flow is attached for the two most inboard fuselage stations in Figs. 13a and 13c. In Figs. 13b and 13d, the leading-edge separation has moved inboard of F.S. = 41.45. This dramatic inboard leading-edge separation shift appears to be consistent with the drag and pitching moment biases discussed earlier with $\alpha = 9$ deg force and moment data trends with Reynolds number. However, there still does not appear to be any clear evidence showing what mechanism is causing this bias.

Trying to understand this biasing effect from another viewpoint, the wing pressure data are given using pressures on or near the wing leading edge as a function of angle of attack. These data are shown in Fig. 14 for the takeoff configuration. The pressure coefficient at $\eta = 0.405$ is representative of the local flow behavior observed on the blunt inboard wing leading edge. The pressure coefficient at $\eta = 0.619$ is representative of the local flow behavior observed near ($\sim$10% of local chord from the leading edge) the sharper outboard wing leading edge. In general, the inboard leading-edge pressures ($\eta = 0.405$) were more sensitive to Reynolds-number changes than the pressures on the outboard wing panel ($\eta = 0.619$). The outboard wing pressures were less sensitive to Reynolds-number changes because of the sharp, outboard wing leading edge. This finding is consistent with that described for the 65-deg delta-wing study.[25]

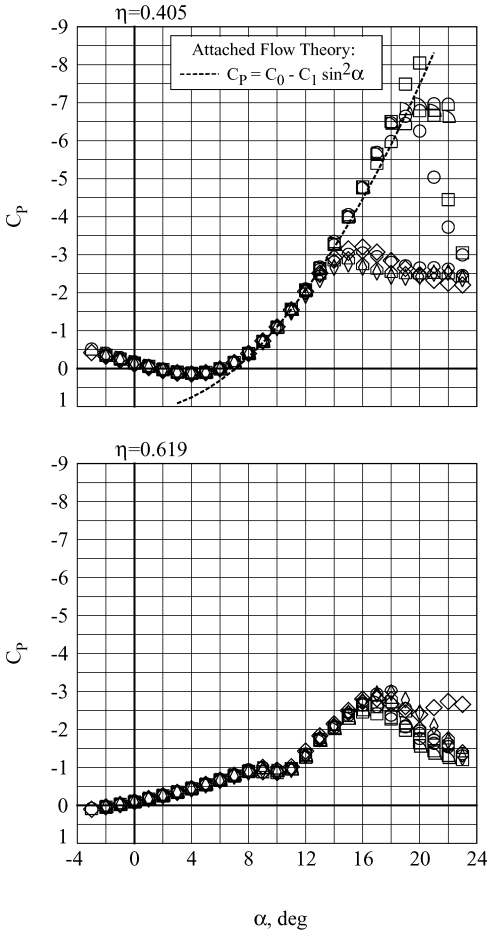

	Rn (millions)	q, psf	T_T, °F
○	8.5	317.	120.
□	10.2	381.	120.
◇	21.6	268.	-201.
▷	21.5	803.	120.
⌂	29.9	818.	-4.
◇	39.9	825.	-90.
◊	49.9	835.	-143.
⌂	90.0	841.	-247.

Fig. 14 Wing leading-edge pressure characteristics for takeoff configuration, $M = 0.30$.

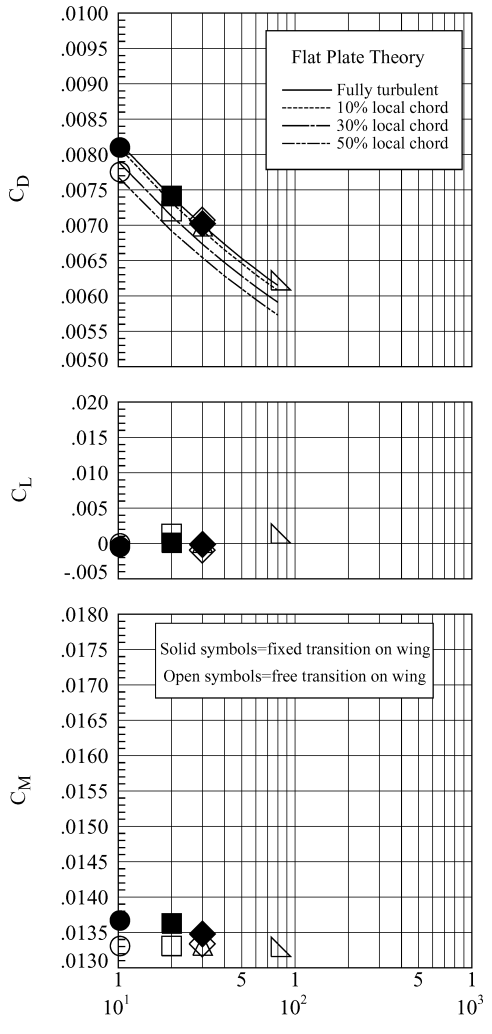

	α, deg	Rn (millions)	q, psf	P_T, psi	T_T, °F
○	1.1	10.2	967.	20.0	121.
□	1.1	20.0	994.	20.6	-97.
◇	1.1	29.8	1003.	20.8	-184.
△	1.1	30.0	1755.	36.3	-52.
◺	1.1	79.6	1797.	37.3	-249.

Fig. 15 Longitudinal coefficient trends with Reynolds number for baseline configuration, near minimum drag, $M = 0.90$ (with aeroelastic correction).

For the blunt inboard wing pressures ($\eta = 0.405$), a distinct grouping of the data also exists. In general, the data for Reynolds numbers 30×10^6 and below show that the leading-edge flow stays attached to greater angles of attack than for higher Reynolds numbers. The higher-Reynolds-number grouping data all depart from the attached flow line at an angle of attack of about 14 deg. This suggests that the inboard movement of the origin of the leading-edge vortex at this station with angle of attack does not depend on Reynolds number. So, these data imply that the leading-edge vortex movement is not a function of Reynolds number.

This grouping behavior is not consistent with typical Reynolds-number effects and points to some biasing effect. Like the force/moment data, there is one exception to this observed trend. The inboard leading-edge pressure data indicate separation onset at a lower angle of attack for a Reynolds number of 21.6×10^6 and a dynamic pressure of 270 psf. However, this same test condition for the force and moment data did not show the same tendency to separate at a lower angle of attack. This observed difference between the pressure and force and moment data for this single test condition occurs because the pressure data were obtained early in the test. Later in the test, the pressure tubing was removed to conduct the force and moment testing alone at similar test conditions. So, the mechanism causing this biasing effect was not always present or effective.

An interesting correlation to tunnel temperature appears, which follows these two pressure data groupings. This correlation also is generally true for the force and moment data except for the one test condition just mentioned. The tunnel temperatures associated with the conditions for premature leading-edge separation were -90°F and colder. This grouping behavior seems to suggest that the test data for the test conditions below -90°F encounters conditions characteristic of laminar boundary-layer separations while the warmer test data experience conditions characteristic of turbulent boundary-layer separations, which can resist separating until higher angles of attack are reached. One mechanism that might explain this type of behavior is if the wing leading-edge surface were colder than the local flow, which might produce a stabilizing effect on the wing leading-edge boundary layer. If this were the case, then the wing leading-edge boundary layers at the cold test conditions would tend to be laminar and more likely to separate at lower angles of attack than if the boundary layer were turbulent.

The similarity of force, moment, and pressure data trends supports the conclusion that an unconfirmed, systematic bias is affecting the takeoff configuration data, but that bias is not Reynolds-number dependent. Though clearly having the bias is not desirable, the Reynolds-number effects within each group (biased, unbiased) are consistent, and observed trends are relevant. As the Reynolds number increases within each group, the drag decrease is consistent with theoretical skin-friction reductions. Also, a Reynolds-number increase for this type of configuration produces increased lift and a more nose-down pitching moment that is characteristic of an increased wing camber effect caused by the reduction of the wing boundary-layer thicknesses.

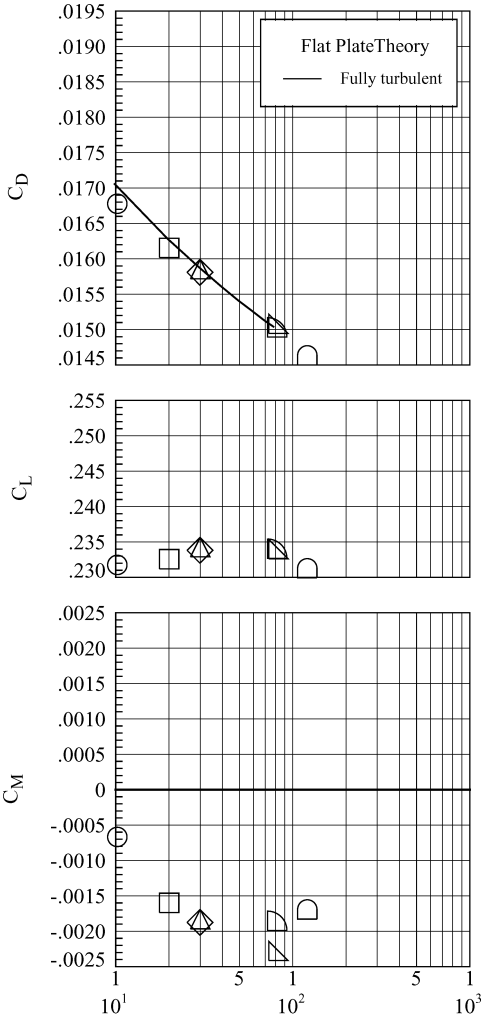

	α, deg	Rn (millions)	q, psf	P_T, psi	T_T, °F
○	5.0	10.2	963.	19.9	120.
□	5.0	20.0	995.	20.6	-97.
◇	5.0	29.9	1005.	20.8	-184.
△	5.0	30.0	1755.	36.3	-52.
◸	5.0	79.5	1802.	37.3	-249.
◱	5.0	80.0	2677.	55.5	-185.
◱	5.0	120.8	2704.	56.1	-250.

Fig. 16 Longitudinal coefficient trends with Reynolds number for transonic cruise configuration, $M = 0.90$ (with aeroelastic correction).

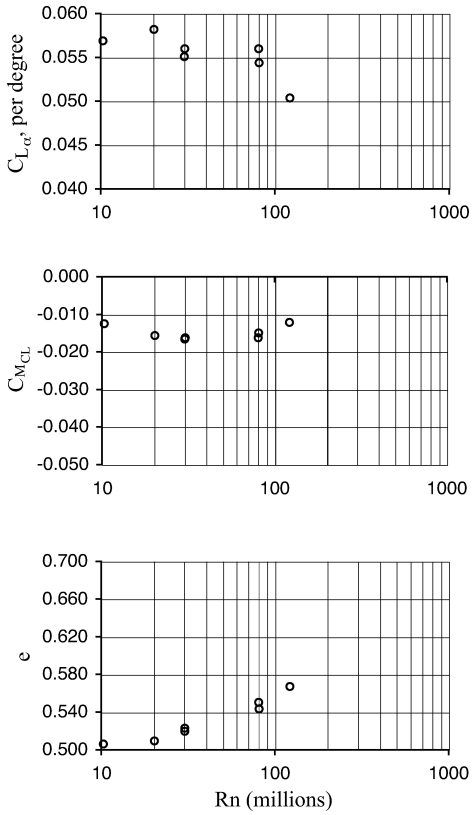

Fig. 17 Lift-curve slope, pitch stability, and Oswald efficiency factor trends with Reynolds number near transonic cruise ($\alpha = 5$ deg), $M = 0.90$ (with aeroelastic correction).

Transonic Conditions

The Reynolds-number effects for the baseline configuration at conditions near minimum drag are presented in Fig. 15. Drag decreased as the Reynolds number increased and is accounted for by theoretical skin-friction drag reduction with Reynolds number. Theoretical skin-friction drag for the configuration was calculated in the same manner discussed earlier in the Low-Speed, High-Lift Conditions section. In Fig. 15, the open symbols represent experimental data acquired allowing free transition of the wing boundary layer; filled symbols represent experimental data acquired with the wing boundary layer transition fixed near the wing leading edge. Several theoretical curves are included where the variable is the extent of laminar flow on the outboard wing panel. All theoretical data were adjusted by a constant increment such that the fully turbulent theoretical curve was anchored to the experimental data for the 80×10^6 Reynolds-number conditions. Increments between the theoretical curves indicate the sensitivity of drag to the boundary-layer transition location on the outboard wing. From these theoretical curves, the change in chordwise extent of the laminar boundary-layer region from fully turbulent to 50% produces a drag level decrease of about five counts. The fully turbulent theoretical skin-friction drag trend aligned well with the experimental drag data obtained with the wing boundary layer tripped at low Reynolds number for the baseline configuration. The agreement between the theoretical and the measured drag trends at this angle of attack demonstrates that the change in drag observed is primarily caused by the reduction in skin-friction drag. The increment between tripped and transition free data at the lower Reynolds number showed the effects of various extents of laminar boundary-layer regions on the outboard wing panels for the baseline configuration. The extent of laminar flow inferred from Fig. 15 is consistent with temperature-sensitive-paint measurements of the boundary-layer transition location on the outboard wing panel.[26,27] The lift and pitching moment trends with Reynolds number presented in Fig. 15 were essentially constant over the range of Reynolds numbers tested at this angle of attack.

The Reynolds-number effects for conditions near the transonic cruise angle of attack are shown in Fig. 16 for the transonic cruise configuration. In general, the coefficient trends exhibit the same behavior as observed at the minimum drag condition. The change in drag coefficient was roughly the same as that seen at the minimum drag condition in Fig. 15, suggesting again that skin-friction reduction remains the primary influence at this higher angle of attack. As with the minimum drag condition, the Reynolds-number effects on lift were not significant near transonic cruise conditions. The Reynolds-number effect on the pitching moment was larger than that observed at the minimum drag conditions. The data show a

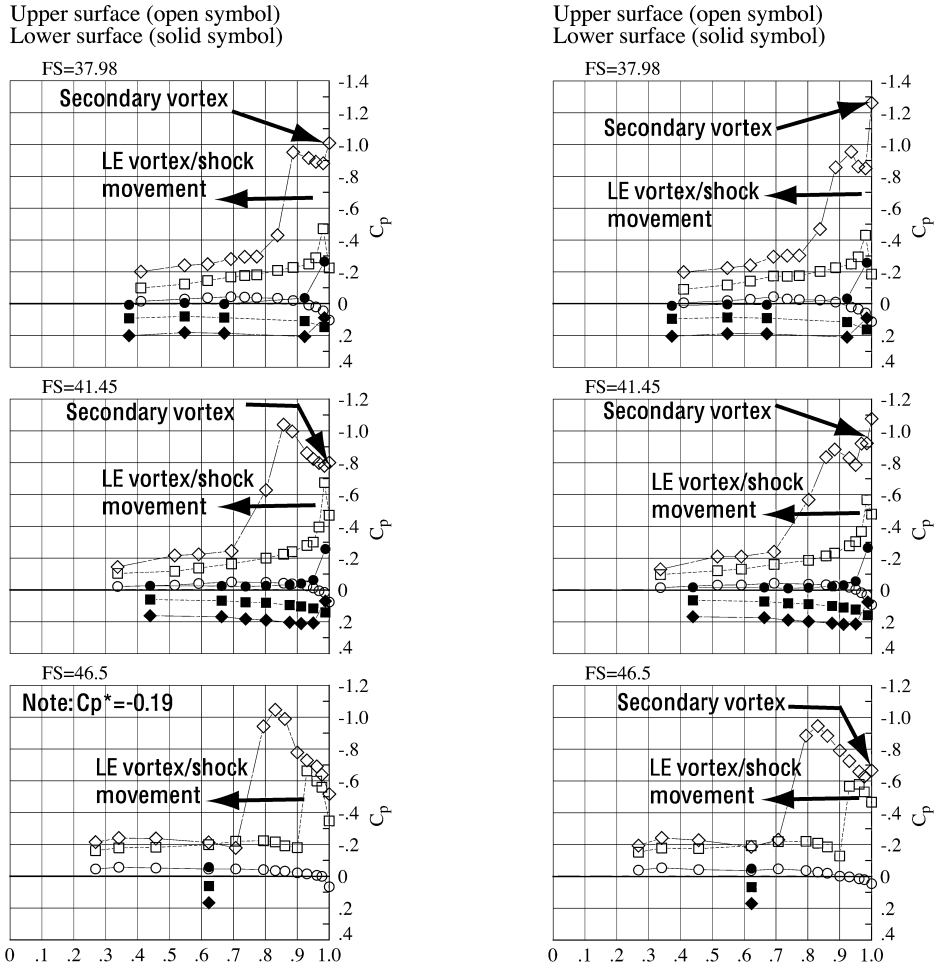

a) $T_T = 120°$F

	α, deg.	C_L	C_m	Rn(millions)	q, psf
○——	-0.1	-0.04	0.01	10.2	967.
□------	4.9	0.23	0.00	10.2	967.
◇—··—	9.9	0.50	0.01	10.2	965.

b) $T_T = -249°$F

	α, deg.	C_L	C_m	Rn(millions)	q, psf
○——	-0.1	-0.05	0.01	79.8	1801.
□------	5.0	0.23	0.01	79.6	1798.
◇—··—	10.1	0.52	0.00	79.3	1794.

Fig. 18 Vortex flow development with α at different Reynolds numbers for the transonic cruise configuration, $M = 0.90$.

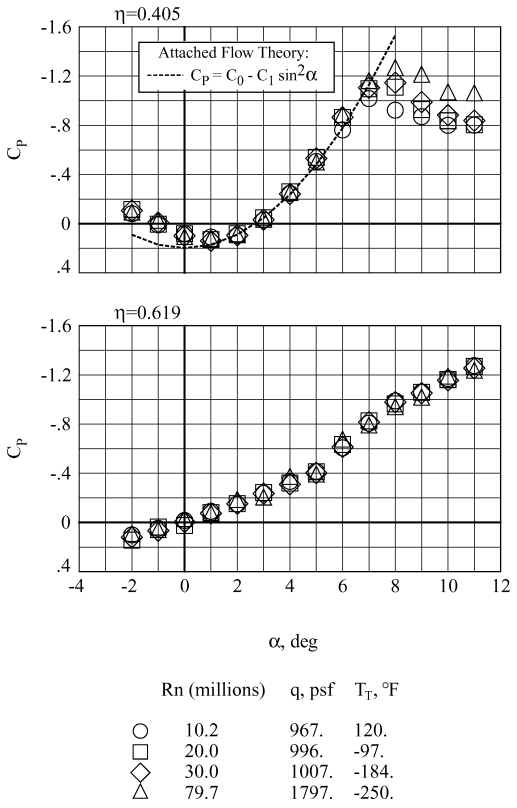

Fig. 19 Wing leading-edge pressure characteristics for transonic cruise configuration, $M = 0.90$.

nose-down change that would require approximately a 0.3-deg stabilizer change (about 1% of the stabilizer deflection range) to compensate for increasing Reynolds number. The increased nose-down character is associated with the increased wing camber effects as the wing boundary layer thins with increasing Reynolds number (see Fig. 11 and the discussion in the Low Speed, High-Lift Conditions section for more details).

The effects of Reynolds number on the lift-curve slope, the pitch stability, and the drag-polar shape for the transonic cruise configuration are shown in Fig. 17. The lift-curve slope for the transonic cruise configuration is essentially constant with a value of approximately 0.055 per degree. The sudden decrease in the lift-curve slope at the highest Reynolds number is believed to be associated with some model/support system dynamics that occurred at this very high dynamic pressure test condition. The negative values of C_{MCL} suggest that this configuration is longitudinally stable. The pitch stability increases as Reynolds number increases. The longitudinal stability increased as the neutral point moved aft by about 0.4% of the mean aerodynamic chord at $\alpha = 5$ deg for the transonic cruise configurations. Again, the highest-Reynolds-number data show a sudden decrease in pitch stability that is believed to be associated with the model/support dynamics issue just mentioned. Note that this Reynolds-number effect on neutral point movement is in a direction opposite to that observed for the static aeroelastic effects. Without adjusting for the static aeroelastic effects, the Reynolds-number effects on pitching-moment behavior are masked.

Finally, to see the change in the drag polar shape with Reynolds number, the trend of the Oswald efficiency factor e with Reynolds number is presented. If this factor is equal to a value of one, then the drag-polar shape is parabolic. For this configuration, this factor increased over the Reynolds-number range from a value of about 0.5 to a value around 0.55. The highest Reynolds-number point has a value of e of about 0.57, but this was associated with a test condition with significant model/support vibrations and can be questionable.

Some spanwise pressure distributions are shown in Fig. 18 for three fuselage stations corresponding to the inboard wing ($\eta \leq 0.522$). The local wing pressure coefficient is plotted vs a spanwise coordinate normalized by the local span at that fuselage station. The nondimensional span coordinate equals zero at the model centerline and one at the wing leading edge.

Each pressure distribution plot in Fig. 18 shows the effect of increasing the angle of attack at a given Reynolds number and dynamic pressure test condition. Also noted on these plots are where vortices/shocks occur and the general inboard movement as the angle of attack increases. The most significant difference noted between the two Reynolds-number conditions is the secondary vortex development as Reynolds number increased. The secondary vortex develops from the reverse flow underneath the primary leading-edge vortex and affects the wing pressures very near the leading edge. Also note the shocks that primarily occur at the highest angle of attack do not appear to be dependent on the change in Reynolds number.

Figure 19 shows the local flow behavior on or near the wing leading edge as a function of angle of attack for the transonic configuration in a manner similar to that already discussed for the takeoff configuration. For all configurations, the pressures were more sensitive to Reynolds-number changes at the higher angles of attack inboard than outboard. The inboard wing leading-edge pressures all depart from the attached flow line at an angle of attack of about 7 deg, which again suggests that the movement of the origin of the leading-edge vortex at this station with angle of attack is not dependent on Reynolds number. Above an angle of attack of 7 deg, the suction levels increase with Reynolds number at each angle of attack. This suction level increase is associated with the development of the secondary vortex separation underneath the primary leading-edge vortex separation with increasing Reynolds number as shown for the inboard wing pressure data in Fig. 18.

Conclusions

Wind-tunnel tests with a supersonic transport model were conducted in a high-Reynolds-number facility across a wide range of Reynolds numbers. The Reynolds numbers spanned from those available in conventional wind tunnels to those near flight conditions at subsonic and transonic Mach numbers. Results were presented that focus on both the Reynolds number and static aeroelastic sensitivities for the longitudinal characteristics of a configuration without a tail. General conclusions are summarized as follows:

1) Static aeroelastic effects are significant. Increasing the dynamic pressure at constant Mach and Reynolds numbers increases the washout of the outboard wing, which in turn contributes to a decrease of the lift-curve slope and decreases pitch stability for the transonic configurations.

2) Adjustments for static aeroelastic effects can be determined and applied to isolate pure Reynolds-number effects. Static aeroelastic effects can mask Reynolds number effects if not adequately isolated. This is particularly evident in the pitching-moment data for all configurations.

3) Reynolds-number effects for the configurations at high-lift conditions are generally small. The lift increases and pitching moment decreases (more nose down) with increasing Reynolds number, which is caused by increased wing camber caused by reductions in the wing boundary-layer thickness at a given angle of attack. The drag trend with Reynolds number is dominated by scaleable skin-friction correlations. The lift-curve slope, the pitch stability, and the drag polar shape for this configuration were relatively insensitive to changes in Reynolds number.

4) At the takeoff condition ($\alpha = 9$ deg) and for all Reynolds numbers, the flow appears to be attached on both the outboard wing ($\eta = 0.619$) and the inboard wing ($\eta = 0.405$). A leading-edge vortex appears to occur on the outboard wing at an angle of attack just above 9 deg. A leading-edge vortex appears to occur at the inboard wing ($\eta = 0.405$) at an angle of attack of about 14 deg, which is well above the takeoff condition. The angle where the leading-edge vortex occurs at these wing stations appears to be Reynolds-number independent.

5) An unknown systematic bias is observed in the force, moment, and pressure data for the high-lift configurations only. The bias is associated with a non-Reynolds-number effect that appears to be

connected with some type of inboard wing leading-edge change that promotes the inboard wing leading-edge separation at a lower angle of attack for certain test conditions. These test conditions were at higher Reynolds numbers, and the freestream temperatures were colder than -90°F. A possible mechanism for this bias might be caused by a colder model surface stabilizing the wing leading-edge boundary layer, which can produce a laminar boundary-layer state at these test conditions that would separate at lower angles of attack. The Reynolds-number effects with and without this bias are consistent.

6) Reynolds-number effects for the configurations at transonic conditions are generally small; lift and the lift-curve slope are Reynolds-number independent, and the pitch stability increases up to 0.4% of the mean aerodynamic chord. The more nose-down pitching moment with increasing Reynolds number occurred as the wing boundary layers thinned and the wing camber became more effective. The drag trend with Reynolds number is dominated by scaleable skin-friction correlations, assuming approximate transition locations are known. Also, the drag polar shape appears to change slightly toward a parabolic shape as the Reynolds number increased.

7) At the transonic cruise condition ($\alpha = 5$ deg) and for all Reynolds numbers, the flow appears to be attached on both the outboard wing ($\eta = 0.619$) and the inboard wing ($\eta = 0.405$). A leading-edge vortex appears to occur on the outboard wing at an angle of attack just above 5 deg. A leading-edge vortex appears to occur at the inboard wing ($\eta = 0.405$) at an angle of attack of about 7 deg. The angle where the leading-edge vortex occurs at these wing stations appears to be Reynolds-number independent.

Acknowledgments

The authors would like to thank our many partners from industry and the staff of the National Transonic Facility for making these tests successful. In particular, we would like to acknowledge Chet Nelson (Boeing), Marvine Hamner (LeaTech, LLC), Susan Williams (NASA, retired), and Bill Goad (NASA, retired) who invested considerable effort over many years toward the development and testing of this model.

References

[1]McKinney, L. W., and Baals, D. D. (eds.), "Wind-Tunnel/Flight Correlation—1981," NASA CP 2225, Nov. 1981.

[2]Haines, A. B., "Scale Effects on Aircraft and Weapon Aerodynamics," AGARD, AG-323, July 1994.

[3]"Boundary-Layer Simulation and Control in Wind Tunnels," AGARD, AR-224, Report of the Fluid Dynamics Panel Working Group 09, April 1988.

[4]Goldhammer, M. E., and Steinle, F. W., Jr., "Design and Validation of Advanced Transonic Wings Using CFD and Very High Reynolds Number Wind Tunnel Testing," International Council of the Aeronautical Sciences, ICAS Paper 90-2.6.2, Sept. 1990.

[5]Lynch, F. T., "Experimental Necessities for Subsonic Transport Configuration Development," AIAA Paper 92-0158, Jan. 1992.

[6]Bushnell, D. M., Yip, L. P., Yao, C. S., Lin, J. C., Lawing, P. L., Batina, J. T., Hardin, J. C., Horvath, T. J., Fenbert, J. W., and Domack, C. S., "Reynolds Number Influences in Aeronautics," NASA TM 107730, May 1993.

[7]Wilhite, A. W., and Shaw, R. J., "An Overview of NASA's High-Speed Research Program," International Council of the Aeronautical Sciences, Paper 112, Aug. 2000.

[8]Nelson, C. P., "Effects of Wing Planform on HSCT Off-Design Aerodynamics," *10th AIAA Applied Aerodynamics Conference*, Technical Paper, Pt. 1, AIAA, Washington, DC, 1992, pp. 285–303.

[9]Wahls, R. A., Owens, L. R., and Rivers, S. M. B., "Reynolds Number Effects on a Supersonic Transport at Transonic Conditions," AIAA Paper 2001-0912, Jan. 2001.

[10]Owens, L. R., and Wahls, R. A., "Reynolds Number Effects on a Supersonic Transport at Subsonic High-Lift Conditions," AIAA Paper 2001-0911, Jan. 2001.

[11]Foster, J. M., and Adcock, J. B., "User's Guide for the National Transonic Facility Research Data System," NASA TM-110242, April 1996.

[12]Williams, M. S., "Experience with Strain Gage Balances for Cryogenic Wind Tunnels," AGARD-R-774, 1989, pp. 19.1–19.14.

[13]Finley, T. D., and Tcheng, P., "Model Attitude Measurements at NASA Langley Research Center," AIAA Paper 92-0763, 1992.

[14]Burner, A. W., Erickson, G. E., Goodman, W. L., and Fleming, G. A., "HSR Model Deformation Measurements from Subsonic to Supersonic Speeds," *1998 NASA High-Speed Research Program Aerodynamic Performance Workshop*, Vol. 1, 1998, pp. 1569–1588; also NASA CP-1999-209692, Vol. 1, Pt. 2, edited by S. Naomi McMillin, Dec. 1999.

[15]Gloss, B. B., "Current Status and Some Future Test Directions for the US National Transonic Facility," *Wind Tunnels and Wind Tunnel Test Techniques*, Royal Aeronautical Society, London, 1992, pp. 3.1–3.7.

[16]Igoe, W. B., "Analysis of Fluctuating Static Pressure Measurements in the National Transonic Facility," NASA TP-3475, March 1996.

[17]Bobbitt, C. W., Hemsch, M. J., and Everhart, J. L., "NTF Characterization Status," AIAA Paper 2001-0755, Jan. 2001.

[18]Fuller, D. E., "Guide for Users of the National Transonic Facility," NASA TM-83124, July 1981.

[19]Braslow, A. L., and Knox, E. C., "Simplified Method for Determination of Critical Height of Distributed Roughness Particles for Boundary-Layer Transition at Mach Numbers from 0 to 5," NACA TN-4363, Sept. 1958.

[20]Wahls, R. A., Adcock, J. B., Witkowski, D. P., and Wright, F. L., "A Longitudinal Aerodynamic Data Repeatability Study for a Commercial Transport Model in the National Transonic Facility," NASA TP-3522, Aug. 1995.

[21]Wahls, R. A., Gloss, B. B., Flechner, S. G., Johnson, W. G., Jr., Wright, F. L., Nelson, C. P., Nelson, R. S., Elzey, M. B., and Hergert, D. W., "A High Reynolds Number Investigation of a Commercial Transport Model in the National Transonic Facility," NASA TM-4418, April 1993.

[22]Al-Saadi, J. A., "Effect of Reynolds Number, Boundary-Layer Transition, and Aeroelasticity on Longitudinal Aerodynamic Characteristics of a Subsonic Transport Wing," NASA TP-3655, Sept. 1997.

[23]Sommer, S. C., and Short, B. J., "Free-Flight Measurements of Turbulent-Boundary-Layer Skin Friction in the Presence of Severe Aerodynamic Heating at Mach Numbers from 2.8 to 7.0," NASA TN-3391, March 1955.

[24]Poll, D. I. A., and Paisley, D. J., "On the Effect of Wing Taper and Sweep Direction on Leading Edge Transition," *The Aeronautical Journal of the Royal Aeronautical Society*, Vol. 89, No. 883, March 1985, pp. 109–117.

[25]Luckring, J. M., "Transonic Reynolds Number and Leading-Edge Bluntness Effects on a 65° Delta Wing," AIAA Paper 2003-0753, Jan. 2003.

[26]Hamner, M. P., "Demystifying Luminescent Paint Technology, A Guide for Non-Developers," AIAA Paper 2001-2981, June 2001.

[27]Hamner, M. P., Popernack, T. G., Jr., Owens, L. R., and Wahls, R. A., "Using Temperature Sensitive Paint Technology," AIAA Paper 2002-0742, Jan. 2002.